

Twisted quadrupole topological photonic crystals

Xiaoxi Zhou^{1,‡}, Zhi-Kang Lin^{1,‡}, Weixin Lu¹, Yun Lai², Bo Hou^{1,†}, Jian-Hua Jiang^{1,†}

¹*School of Physical Science and Technology, and Collaborative Innovation Center of Suzhou Nano Science and Technology, Soochow University, 1 Shizi Street, Suzhou, 215006, China*

²*National Laboratory of Solid State Microstructures, School of Physics, and Collaborative Innovation Center of Advanced Microstructures, Nanjing University, Nanjing 210093, China*

[#]These authors contributed equally to this work.

[†]Correspondence and requests for materials should be addressed to jianhujiang@suda.edu.cn (Jian-Hua Jiang), houbo@suda.edu.cn (Bo Hou).

Abstract

Topological manipulation of waves is at the heart of the cutting-edge metamaterial research. Quadrupole topological insulators were recently discovered in flux-threading lattices as higher-order topological insulators which give access to topological wave trapping at both the edges and corners. Photonic crystals, lying at the boundary between continuous media and discrete lattices, however, are incompatible with the present quadrupole topological theory. Here, we unveil quadrupole topological photonic crystals triggered by a twisting degree-of-freedom. Using a topologically trivial photonic crystal as the motherboard, we show that twisting induces quadrupole topology without flux-threading. The twisting-induced crystalline symmetry enriches the edge polarization structure, leading to anomalous quadrupole topology. Versatile edge and corner phenomena are observed by tuning the twisting angle which controls simultaneously the photonic band gap and the Wannier gap. Our study paves the way toward topological twist-photonics and shed light on quadrupole topology in the quasi-continuum regime for phonons, electrons, and polaritons.

Introduction

The discovery of higher-order topology opens a new horizon in the study of topological physics [1-26] where crystalline symmetry plays a crucial role. Higher-order topological insulators [1-26] are intriguing symmetry-protected topological phases where topology and symmetry manifest themselves in multiple dimensions, unveiling a paradigm beyond the conventional bulk-edge correspondence [27, 28]. For instance, two-dimensional (2D) quadrupole topological insulators (QTIs) [1, 4] host one-dimensional (1D) gapped edge states and topologically-protected zero-dimensional (0D) corner states emerging in the common spectral gap of the bulk and edge. The concept of QTI generalizes the conventional Bloch band topology to the Wannier band topology [1, 4] which is described by the so-called “nested Wannier bands”. A π -flux lattice model for QTIs is proposed in Ref. [1] which was later realized in experimental systems based on mechanical metamaterials [10], electric circuits [11, 12], and coupled optical ring resonators [19]. However, the π -flux lattice picture is incompatible with conventional photonic crystals which lie at the boundary between continuous media and discrete-lattice systems. A straightforward generalization of the π -flux lattice to photonic crystals would fail since there is no mechanism for flux-threading. On the other hand, quadrupole topological photonic crystals, where light-matter interaction can be much enhanced by topological light-trapping on the edges and corners at subwavelength scales, are on demand for topological photonics in the nonlinear and quantum regimes.

Recently, twisting has been discovered as an invaluable approach toward exotic states of matter with nontrivial topology, strong correlation, or superconductivity in 2D van der Waals materials. However, the power of twisting has not been fully unleashed in photonics where twisting is, in fact, experimentally more accessible than in electronic systems. Here, we propose theoretically and observe experimentally an anomalous QTI (AQTI) phase of photons using the twisting degree-of-freedom. Exploiting a common square-lattice photonic crystal (PhC) as the motherboard, we show that a particular twisting deformation can induce the AQTI phase when the mirror symmetries are removed while the glide symmetries emerge. In AQTIs, the flux-threading mechanism is not needed, and the system is not based on tight-binding models but rather on the emergence of the quadrupole topology due to the glide symmetries in the quasi-continuum regime. In this regime, the photonic band gap is formed

due to the multiple Bragg scattering mechanism instead of tight-binding couplings between local resonances. Moreover, the twisting approach leads to photonic crystals with “anomalous quadrupole topology” which differs fundamentally from the conventional quadrupole topology as follows: First, the twisting induced nonsymmorphic symmetry doubles the band representation, hence at least four bands are needed below the quadrupole topological band gap. Second, in the Wannier representation, four nondegenerate Wannier bands are required as the minimal description of the anomalous quadrupole topology. Third, such enlarged Wannier representation enriches the edge polarization structure which now consists of a topological (quantized) sector and a trivial (non-quantized) sector.

In experiments, we use 2D subwavelength photonic crystals made of Al_2O_3 cylinders to realize the photonic AQTIs via twisting the unit-cell structure. Using the electromagnetic near-field scanning methods, we directly measure and visualize the photonic wavefunctions of the bulk, edge and corner states. Versatile manipulation of the edge and corner states are revealed in both simulation and experiments by tuning the twisting angle. Exploiting such controllability, we demonstrate that when the frequencies of the edge and corner states are tuned close, their mutual couplings enable excitation of corner states via the edge states. These findings reveal rich phenomena of photonic edge and corner states using twist-induced topology and may inspire future developments of higher-order topological photonics beyond the conventional bulk-edge correspondence [29-48].

Results

System and symmetry

The 2D square-lattice PhC has four identical cylinders made of Al_2O_3 (radius 0.25 cm) in each unit-cell. The lattice constant is $a = 2$ cm. The dielectric PhC is placed in a 2D cavity formed by metallic cladding above and below, where the transvers-magnetic harmonic modes (i.e., the modes with electric fields along the z direction) dominate the photonic bands at low frequencies. We start with a configuration where the four cylinders are located at the positions of $(\pm \frac{a}{4}, \pm \frac{a}{4})$ and the unit-cell has C_{4v} point-group symmetry. By twisting the four cylinders along the dashed lines as illustrated in Fig. 1a, the crystalline symmetry is reduced to the

nonsymmorphic group $P4g$ which contains the two glide symmetries, $G_x := (x, y) \rightarrow (\frac{a}{2} - x, \frac{a}{2} + y)$ and $G_y := (x, y) \rightarrow (\frac{a}{2} + x, \frac{a}{2} - y)$, the four-fold rotation symmetry, C_4 , and the inversion symmetry $I := (x, y) \rightarrow (-x, -y)$. Note that the two glide symmetries do not commute with each other, $G_x G_y \neq G_y G_x$, since $G_x G_y := (x, y) \rightarrow (-x, a - y)$ and $G_y G_x := (x, y) \rightarrow (a - x, -y)$. Here, the twist is not a pure rotation, but is designed to preserve the glide symmetries.

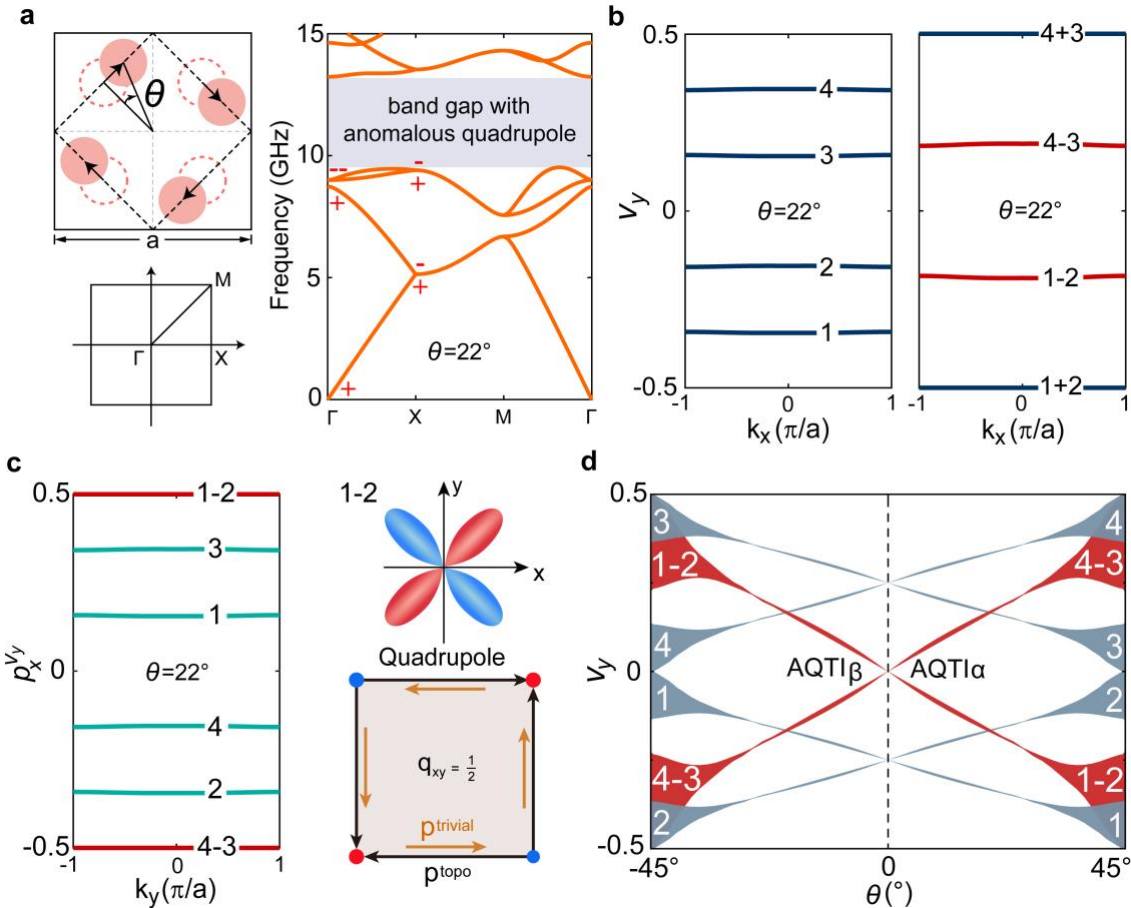


Figure 1 | Photonic anomalous quadrupole topological insulators. **a**, Left: Unit-cell structure and Brillouin zone. Twisting is along the dashed lines with θ denoting the (clockwise) twisting angle. Right: Photonic band structure for $\theta = 22^\circ$. The photonic band gap between the fourth and fifth bands exhibits anomalous quadrupole topology. **b**, Wannier bands and their combinations. **c**, Nested Wannier bands and the quantized quadrupole moment in the Wannier sector “1-2” (the right-upper panel). The right-lower panel illustrates that the edge polarizations include the topological

contribution with the quadrupole geometry and the trivial contribution with C_4 rotation symmetry.

d, Evolution of the Wannier bands with the twisting angle θ .

Photonic bands

We now point out the consequences of the glide symmetries on the photonic bands. First, the glide symmetries lead to double degeneracy of photonic bands at the Brillouin zone boundaries (i.e., the MX and MY lines; they are equivalent since the system has the C_4 rotation symmetry). This can be illustrated via the anti-unitary operators $\Theta_i \equiv G_i \mathcal{T}$ ($i = x, y$). Here, \mathcal{T} is the time-reversal operator which is explicitly the complex conjugation operator for the electromagnetic wavefunctions. One finds that $\Theta_x^2 \psi_{n,\vec{k}} = -\psi_{n,\vec{k}}$ if $k_x = \pi/a$, and $\Theta_y^2 \psi_{n,\vec{k}} = -\psi_{n,\vec{k}}$ if $k_y = \pi/a$, for any photonic Bloch wavefunction $\psi_{n,\vec{k}}$ with n and \vec{k} being the band index and the wavevector, respectively. Similar to the Kramers theorem, these algebraic properties give rise to the double degeneracy for *all* photonic bands at the MX and MY lines. In addition, the inversion operator, \mathcal{I} , and the anti-unitary operator, Θ_x (Θ_y), anti-commute at the X (Y) point. Therefore, the doubly degenerate bands at the X (Y) point always include an odd-parity band and an even-parity band [See Fig. 1a; See Supplementary Note 1 for the proof]. From the parity-inversion between the Γ and X (Y) points [see Fig. 1a], we conclude that the Wannier dipole is quantized to $\vec{P} = (\frac{1}{2}, \frac{1}{2})$ for the partial photonic band gap between the second and the third bands, whereas the Wannier dipole is quantized to $\vec{P} = (0,0)$ for the complete photonic band gap between the fourth and the fifth bands. The vanishing dipole polarization of the complete photonic band gap provides a necessary condition for the emergence of the quadrupole topology.

The photonic band structure for the PhC with $\theta = 22^\circ$ is shown in Fig. 1a which exhibits a large photonic band gap (30%) between the fourth and fifth bands, ranging from 9.46 GHz to 13.2 GHz, corresponding to a subwavelength regime (i.e., the structure features and the lattice constant are smaller than the wavelengths in vacuum). Throughout this paper, the permittivity of the dielectric cylinders is taken as $\epsilon = 6.2$ for the 2D simulation to best represent the experimental measurements in the quasi-2D systems (See Supplementary Note 2 for detailed comparison between the 2D approximation and the 3D simulation).

Quadrupole topology

We illustrate below that such a photonic band gap carries the anomalous quadrupole topology. The underlying physics of the AQTI phase does not rely on any tight-binding model, but can be directly characterized through the “nested Wannier bands” approach [1, 4] using the photonic wavefunctions from the first-principle calculations (see Fig. 1). The nontrivial quadrupole topology in the $P4g$ PhC is revealed as the symmetry-enforced quantization of the quadrupole moment in the Wannier representation due to the glide symmetries (See Supplementary Note 3 for the proof).

According to Refs. [1] and [4], nontrivial quadrupole topology requests the following key elements: First, the gapped Wannier bands and the vanishing total polarization, meaning that the Wannier centers are away from 0 or $\frac{1}{2}$ and come in pair with both positive and negative values, i.e., $(-\nu, \nu)$ with $0 < \nu < \frac{1}{2}$. Second, the finite, quantized quadrupole moment as manifested in the nontrivial, quantized Wannier sector polarizations. The former is a necessary condition for the latter. In previous theories [1, 4], the first condition is realized via the flux-threading mechanism which leads to the non-commutative mirror symmetries. Without the flux-threading, the commutative mirror symmetries guarantee gapless Wannier bands and hence forbid the quadrupole topology. In our flux-free systems, the motherboard PhC has commutative mirror symmetries and hence gapless Wannier bands. When the mirror symmetries are removed by twisting, the non-commutative glide symmetries give rise to the quadrupole topology.

The Wannier bands are calculated from the photonic Bloch wavefunctions using the Wilson-loop method. The Wilson-loop operator along, e.g., the y direction is defined as [1, 4, 49]

$$\hat{W}_{y,\mathbf{k}}(k_x) = \mathcal{T}_P \exp[i \oint \hat{A}^y(\mathbf{k}) dk_y], \quad (1)$$

where the subscript y and \mathbf{k} specify, respectively, the direction and the starting point of the loop. $\hat{A}^y(\mathbf{k})$ is the matrix (non-Abelian) formulation of the photonic Berry connection with its matrix element written as $A_{nm}^y(\mathbf{k}) = i \langle E_m(\mathbf{k}) | \partial_{k_y} | E_n(\mathbf{k}) \rangle$ where $|E_n(\mathbf{k})\rangle$ is the periodic part of the photonic Bloch wavefunction for the electric field. The ket-bra symbols and the inner product for

the photonic wavefunctions are defined in the Supplementary Note 4. The first four photonic bands below the topological band gap are numerated by $n, m = 1, 2, 3, 4$. \mathcal{T}_P represents the path-ordering operator along a closed loop in the Brillouin zone (BZ). Here, the Wilson-loop path has fixed k_x , but with k_y traversing the whole region of $[0, \frac{2\pi}{a}]$.

The Wilson-loop operator is diagonalized to obtain the Wannier bands, $\widehat{W}_{y,\mathbf{k}} \xi_{y,\mathbf{k}}^j = e^{2\pi i v_y^j(k_x)} \xi_{y,\mathbf{k}}^j$ for $j = 1, 2, 3, 4$. The j -th Wannier band is explicitly the dependence of the Wannier center $v_y^j(k_x)$ on the wavevector k_x [see Fig. 1b]. The eigenvectors $\xi_{y,\mathbf{k}}^j$ are used to construct the Wannier band bases [1], $|w_j(\mathbf{k})\rangle = \sum_{n=1}^4 [\xi_{y,\mathbf{k}}^j]^n |E_n(\mathbf{k})\rangle$ with $[\xi_{y,\mathbf{k}}^j]^n$ denoting the n -th element of the eigenvector $\xi_{y,\mathbf{k}}^j$. The Wannier band bases can be regarded as the Wannier “wavefunctions” from which the topology of the Wannier bands can be defined. For instance, the polarizations of the gapped, non-degenerate Wannier bands are given by $p_{x,j}^{v_y}(k_y) = \frac{1}{2\pi} \oint \tilde{A}_j^x(\mathbf{k}) dk_x$ where $\tilde{A}_j^x(\mathbf{k}) = i\langle w_j(\mathbf{k}) | \partial_{k_x} | w_j(\mathbf{k}) \rangle$ is the Berry connection for the j -th Wannier band. The Wannier band polarizations, $p_{x,j}^{v_y}(k_y)$, which characterize the topological properties of the Wannier bands, are also termed as the “nested Wannier bands” [1] (see Supplementary Note 4 for calculation details).

Figure 1b shows that there are four Wannier bands that are non-degenerate and gapped, distributing symmetrically in the positive and negative regions. According to their signs, the two negative Wannier bands form a group (denoted as the “group I”), while the two positive Wannier bands form another group (denoted as the “group II”). Physically, the group I and the group II represent Wannier centers localized at the lower and upper sides of the unit-cell center, respectively [4]. When a large but finite crystal is considered, the edge states at the lower and upper edges are connected to the Wannier orbitals in the group I and group II, respectively [1]. Accordingly, the Wannier band polarizations, $P_{x,j}^{v_y} = \frac{1}{2\pi} \int p_{x,j}^{v_y}(k_y) dk_y$, in the group I (II) characterize the polarization of the lower (upper) edge [1] induced by the bulk photonic band properties.

Unlike the conventional QTIs with two Wannier bands, the four Wannier bands in AQTIs enable rich polarization structures for the edges. Let’s consider the lower edge which is

associated with the Wannier bands 1 and 2 (i.e., the group I). The sum of the polarizations of these two Wannier bands, $P_x^{\nu_y, I} = P_{x,1}^{\nu_y} + P_{x,2}^{\nu_y}$, give the total edge polarization. Interestingly, none of these polarizations, $P_{x,1}^{\nu_y}, P_{x,2}^{\nu_y}$, nor the total edge polarization $P_x^{\nu_y, I}$ is quantized. However, the glide symmetries lead to quantization of the edge polarization in the “difference sector”, $P_x^{\nu_y, I_{\text{topo}}} = P_{x,1}^{\nu_y} - P_{x,2}^{\nu_y} = \frac{1}{2}$ [see Fig. 1c], because of the following symmetry constraint [see Supplementary Note 3 for the proof]

$$P_x^{\nu_y, I_{\text{topo}}} \stackrel{G_x}{\Leftrightarrow} -P_x^{\nu_y, I_{\text{topo}}} \bmod 1.$$

Since the x and y directions are equivalent for the $P4g$ crystal, one has $P_y^{\nu_x, I_{\text{topo}}} \stackrel{G_y}{\Leftrightarrow} -P_y^{\nu_x, I_{\text{topo}}} \bmod 1$ and $P_y^{\nu_x, I_{\text{topo}}} = P_{y,1}^{\nu_x} - P_{y,2}^{\nu_x} = \frac{1}{2}$. The quadrupole polarization in this particular sector is then quantized, $q_{xy} = 2P_x^{\nu_y, I_{\text{topo}}} P_y^{\nu_x, I_{\text{topo}}} = \frac{1}{2}$, which signals the quadrupole topology and dictates the emergence of the gapped edge states and in-gap corner states. The total edge polarization contains both the quadrupole contribution and the trivial contribution, $P_x^{\nu_y, I} = P_x^{\nu_y, I_{\text{topo}}} + P_x^{\nu_y, I_{\text{trivial}}}$. Note that the trivial polarization, $P_x^{\nu_y, I_{\text{trivial}}} = 2P_{x,2}^{\nu_y}$ does not contribute to the corner charge and hence does not change the bulk-corner correspondence in quadrupole topology [see Fig. 1c; see the detailed analysis in Supplementary Note 5]. This is because for each corner the inward trivial edge polarization is equal to the outward trivial edge polarization due to their C_4 symmetric configuration. The non-quantized total edge polarization is consistent with the fact that there is no mirror symmetry to quantize the edge polarization. The emergence of the quadrupole topology in the combinations “1-2” and “4-3” is also consistent with the fact that only the combinations “1-2” and “4-3” yield gapped Wannier bands [see Fig. 1b] which is necessary for the quadrupole topology.

We find that for the case with a negative twisting angle, which is connected to the case with the opposite twisting angle through a mirror transformation with respect to the x or y axis, the bulk-induced edge polarization for both the first and the second Wannier bands, $P_{x,1}^{\nu_y}$ and $P_{x,2}^{\nu_y}$, flip sign. Thus, both the topological and trivial bulk-induced edge polarizations switch sign, i.e., $P_x^{\nu_y, I_{\text{topo}}} = P_y^{\nu_x, I_{\text{topo}}} = -\frac{1}{2}$. Nevertheless, the quadrupole moment remains as $q_{xy} = \frac{1}{2}$. We denote

the topological phase with negative θ as AQT β , whereas the topological phase with positive θ as AQT α [see Fig. 1d].

The evolution of the Wannier bands with the twisting angle θ is shown in Fig. 1d. The Wannier bands in the combinations “1-2” and “4-3” become gapless in the limits: $\theta \rightarrow 45^\circ$ and $\theta \rightarrow 0$ where the mirror symmetries are recovered. These properties agree with the observation in Ref. [4] that mirror symmetries without flux-threading lead to gapless Wannier bands and forbid quadrupole topology. In addition, the photonic band gap closes in the limit of $\theta \rightarrow 45^\circ$. The twisting angle thus controls effectively both the Wannier band gap and the photonic band gap.

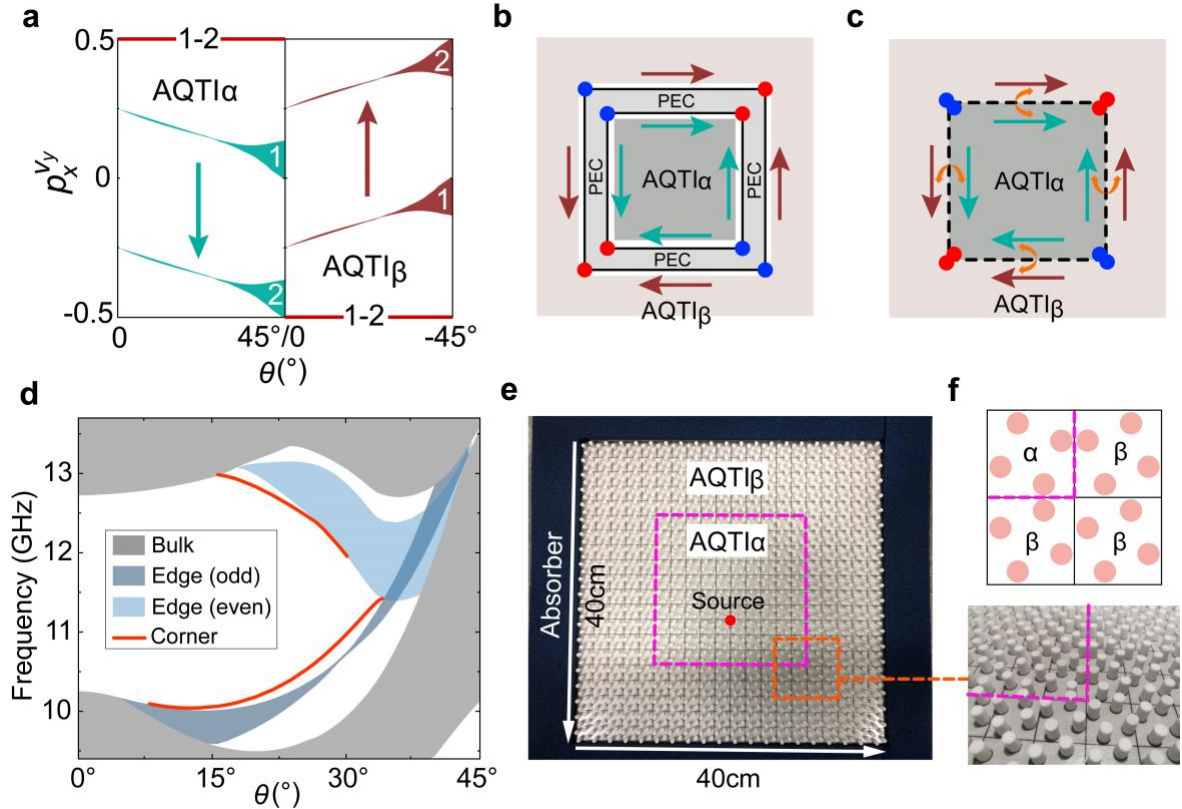


Figure 2 | Bulk, edge and corner states modulated by the twisting angle. **a**, Nested Wannier bands for AQT α and AQT β as functions of the twisting angle. The arrows indicate the directions of the topological edge polarization for the two PhCs. **b**, Schematic illustration of the edge and corner states for a box-like structure where the central region is the AQT α and the outside region is the AQT β . In between them is the region with the PEC boundaries. The arrows represent edge states and their

topological polarizations, while the red and blue dots represent the corner states. **c**, The box-like structure without the PEC boundaries. The boundary between the two PhCs is denoted by the black dashed lines. Orange double arrows represent interactions between the edge states from the two sides of the boundary. **d**, Evolution of the bulk, edge (including odd and even edge modes) and corner states with the twisting angle θ . The bulk spectrum is obtained from the unit-cell calculation, while the edge and corner spectra are from the ribbon- and box-like (as shown in **c**) supercell calculations, respectively. **e**, The experimental set-up that realizes **c**. **f**, The detailed structure of the PhCs at the corner. Upper panel: top-down view; Lower panel: bird-view photograph.

Within the $P4g$ space group, we did not find any PhC with gapped Wannier bands but vanishing quadrupole topology. Nevertheless, we can exploit the two PhCs with opposite twisting angles to construct a supercell with the edge and corner states. The scenario is illustrated in Figs. 2b and 2c. If a perfect-electric-conductor (PEC) boundary is used to enclose the AQT α and AQT β as illustrated in Fig. 2b, then the topological edge (corner) states emerge at the boundaries (corners) for both types of PhCs [See Supplementary Note 6 for the spectra and wavefunctions of the edge and corner states]. Note that in Fig. 2b the outer boundaries of the AQT α have the same edge polarization configurations as the inner boundaries of the AQT β (the arrows label the topological edge polarizations). This is because the two PhCs have opposite bulk-induced edge polarizations for the outer boundaries, and the outer boundaries have opposite edge polarization configurations as for the inner boundaries. However, the use of PEC is incompatible with our experimental system based on the transvers-magnetic harmonic modes and thus the PEC boundaries must be avoided. and hence do not cancel with each other. The removal of the PEC boundaries enables the coupling between the edge states from the outer boundaries of the AQT α and those from the inner boundaries of the AQT β (see Fig. 2c). With such couplings, the hybridized edge states form the symmetric and anti-symmetric (i.e., even-parity and odd-parity) edge modes (see Supplementary Note 7 for their wavefunctions), because the edge boundaries are mirror symmetric. The evolution of the bulk, edge and corner spectra with the twisting angle θ for the set-up in Fig. 2c is presented in Fig. 2d. The corresponding experimental system is illustrated in Figs. 2e and 2f.

The coupling between the edge states is reflected by the splitting between the symmetric and anti-symmetric modes, which can be controlled by the twisting angle θ effectively, as shown in Fig. 2d. When θ approaches 0, because of the closing of the Wannier band gap, and also because the two PhCs with opposite twisting angles are tuning into the same geometry, the edge states merge into the bulk. Figure 3a shows that the wavefunctions of the odd-parity edge states become weakly confined on the edges and gradually become delocalized, as the twisting angle approaches 0. Similar tuning of the even-parity edge states is observed (see Supplementary Figure 10). In the other limit, with the twisting angle approaching 45° , the close of the bulk band gap also leads to delocalization and annihilation of the edge states. However, in this process, the edge band gap closes before the bulk band gap closes [see Fig. 2d]. Later, these edge states merge into the bulk states (see Fig. 3a and the Supplementary Note 8).

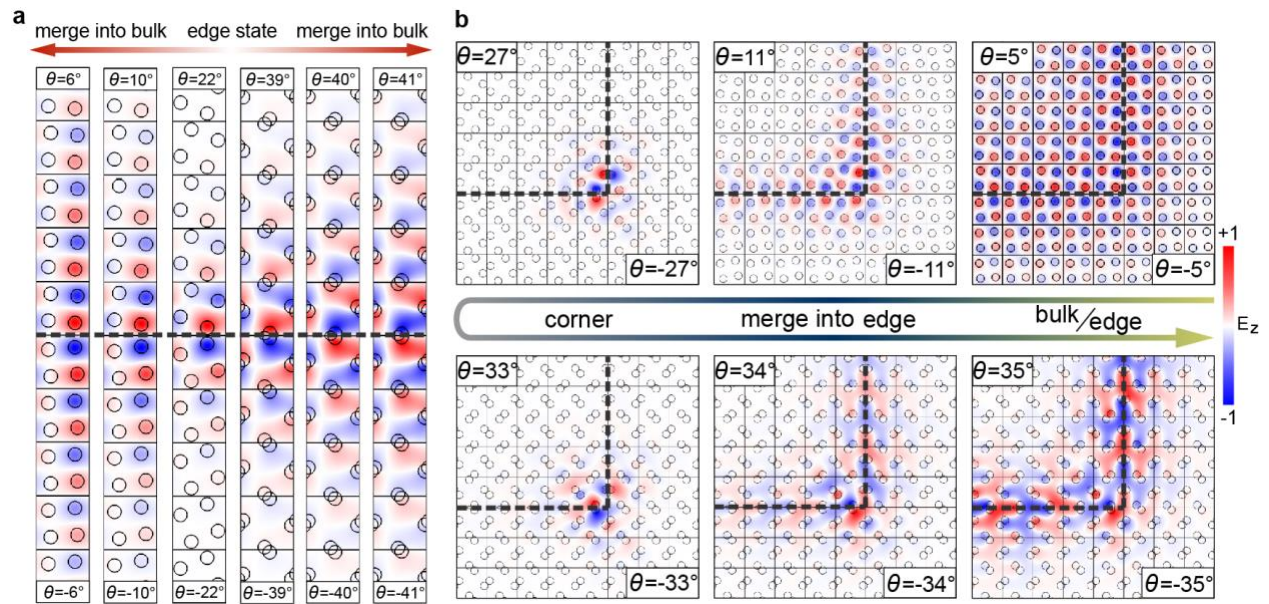


Figure 3 | Controlling the edge and corner states by tuning the geometry. **a**, Evolution of the odd edge states at $k_x = 0$ with the twisting angle θ . Similar variation of the even edge states is presented in the Supplementary Figure 10. The edge states merge into the bulk in both small and large θ limit. **b**, Evolution of the lower-frequency corner states with the twisting angle θ . The variation of the higher-frequency corner states is presented in the Supplementary Figure 10. Note that the corner states merge into the edge in both the small and large θ limit. For the small θ limit, the corner state evolves into the odd edge state, whereas in the large θ limit, it evolves into the even edge state.

The corner states also experience strong modulation when the twisting angle is tuned. Fig. 3b shows the controllability of the lower-frequency corner states by the twisting angle. With $\theta \rightarrow 0$, the corner states first merge into the edge states and then into the bulk states. When θ approaches 45° , the corner states merge into the edge states as well due to the edge band gap closes. Interestingly, when $\theta \rightarrow 0$, the lower-frequency corner states merge into the odd-parity edge states, whereas when $\theta \rightarrow 45^\circ$ the lower-frequency corner states merge into the even-parity edge states. For the higher-frequency corner states, we find that it can be transferred into the bulk states by reducing the twisting angle. In the other direction, by increasing the twisting angle, the higher-frequency corner states can merge into the even-parity edge states. These findings indicate that twisting can be used as an efficient tool to transfer photonic states from 0D corner states to 1D edge states or 2D bulk states, in reconfigurable PhCs.

Experiments

The experimental set-up used to verify the physics elaborated above is shown in Fig. 2e where the box-like PhC structure realizes the schematic illustration in Fig. 2c. The whole structure contains 20×20 unit-cells (including 10×10 unit-cells for AQT α in the center and other 300 unit-cells for the AQT β at the outside). Electromagnetic waves are excited in the AQT α region and absorbed by the absorber outside the structure. The detection for the bulk, edge and corner modes are realized by three probes located in the bulk region of AQT α , on the edge and at the corner, separately. They are termed as the bulk-probe, edge-probe and corner-probe, respectively.

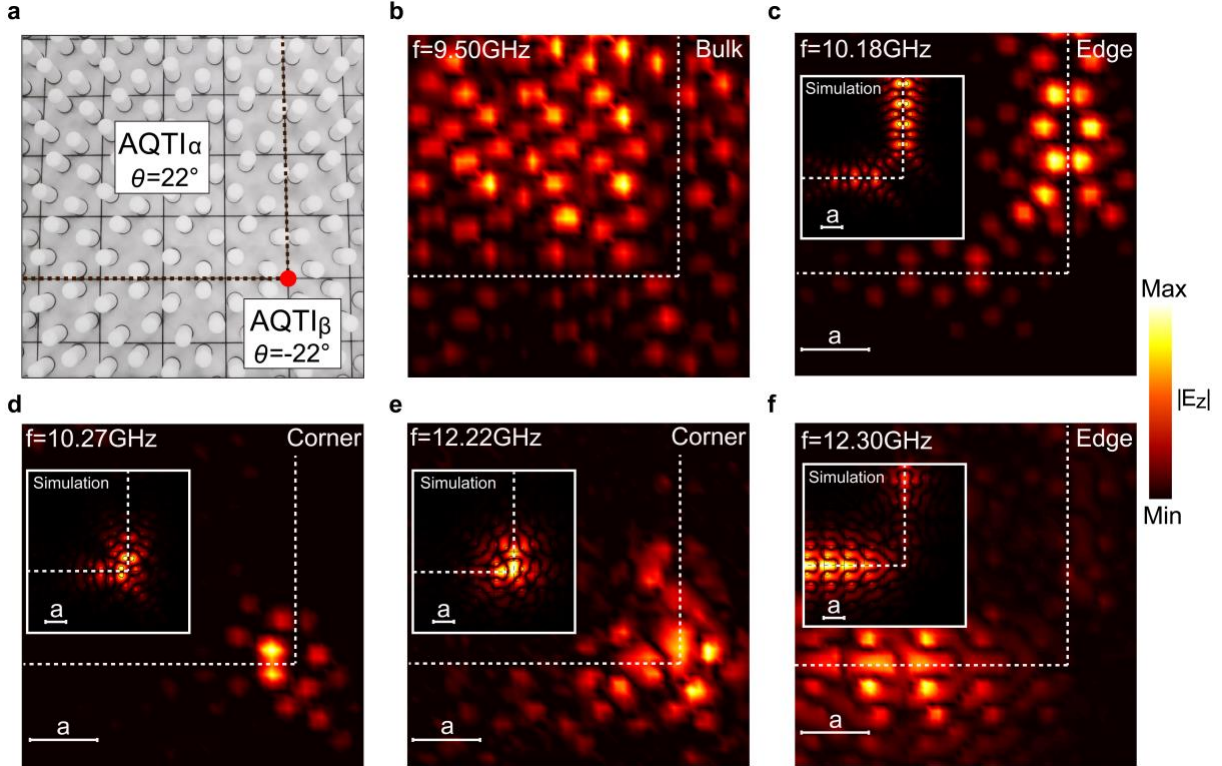


Figure 4 | Measuring the photonic wavefunctions for the bulk, edge and corner states. **a**, Photograph of a part of the box-like structure used in the experiments with $|\theta| = 22^\circ$. The corner is denoted by the red dot. **b-f**, The measured electric field profiles for the bulk (**b**), edge (**c** and **f**) and corner (**d** and **e**) states. Insets: simulation results with a smaller scale. The lattice constant is labeled by the white scale bar. For all figures, the edge boundaries are denoted by the white dashed lines.

We measure the photonic wavefunction of the bulk, edge and corner states by near-field scanning of the electromagnetic field [See Materials and Methods]. The results are presented in Fig. 4 for a part of the box-like structure with $\theta = 22^\circ$. The photograph of the PhC structure is shown in Fig. 4a. The boundary between the two types of PhCs is illustrated by the dashed lines, while the corner is denoted by the red dot. From low frequency to high frequency, we show five typical photonic wavefunctions: the bulk state at 9.50 GHz [Fig. 3b], the edge states at 10.18 and 12.30 GHz [Figs. 3c and 3f], the corner states at 10.27 and 12.22 GHz [Figs. 3d and 3e]. The real-part of the corner wavefunctions from both the simulation and the experiments are shown in Supplementary Note 9. In all these studies, the measured electric field distributions agree well

with the numerical simulation. These results directly visualize the corner and edge states, and confirm the physics picture elaborated in the previous section.

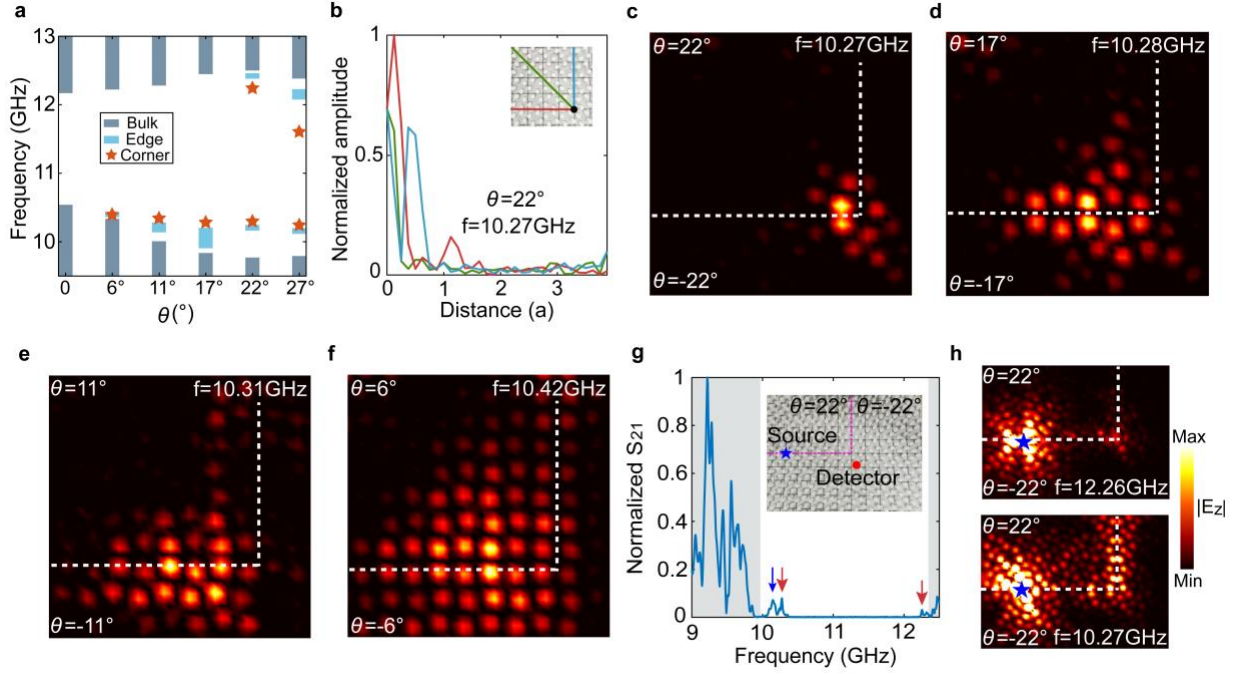


Figure 5 | Measuring the corner states and their evolution with the twisting angle. **a**, The spectral regions for the bulk, edge and corner states for various twisting angles. **b**, Measurement of the electric field profiles along three directions (illustrated by the red, green and blue lines in the inset) for the corner state (resonant frequency 10.27 GHz) at $\theta = 22^\circ$. **c-f**, Evolution of the wavefunction of the corner states with the twisting angle. **g**, Pump-probe spectroscopy for the set-up with the source at the edge and the detector close to the corner (see the inset) for $\theta = 22^\circ$. **h**, The measured electric field profile for two corner states at resonant frequencies 10.27 GHz and 12.26 GHz, respectively.

We then study the scattering coefficient (S_{21}) spectrum of the bulk-probe, edge-probe and corner-probe, which give effectively the local density of states in the bulk, edge and corner regions. The pump-probe spectroscopies for various twisting angles θ are presented in Supplementary Note 10. We extract from the S_{21} spectra the frequency range for the bulk, edge and corner modes. The results are shown in Fig. 5a for six different twisting angles θ from 0° to

27°, which agree quite well with the simulation in Fig. 2d. Larger twisting angles are avoided because of the overlap of the Al₂O₃ cylinders at the unit-cell boundaries. To confirm the fully localized nature of the corner states, we measure the electric field profile of the corner state around one of the corners. Fig. 5b presents the electric field profiles measured along three lines (the red, blue and green lines as indicated in the inset) for $\theta = 22^\circ$ at the corner mode frequency of 10.27 GHz. The results show that the photonic wavefunction is well-localized at the corner and decays rapidly in all three directions, which confirm the observation of corner states as photonic bound states.

The evolution of the lower-frequency corner state with the twisting angle θ is studied in details in Figs. 5c-5f with θ varying from 22° to 6°. These figures show clearly that the corner state gradually evolves from strongly localized to weakly localized. The corner state eventually merges into the bulk band and becomes a bulk state in the limit of $\theta \rightarrow 0$.

In the existing studies on higher-order topological insulators, the corner states are spectrally well-separated from the edge and bulk states [1, 4, 9, 11-13, 19, 20, 25]. Such isolation makes it hard to utilize them for functional devices. Here, we show that, thanks to the tunable nature of the corner states in our PhCs, the frequency of the corner states can be tuned to be close to the edge states and thus enable their mutual coupling in finite-sized systems. In experiments, we choose the set-up with the twisting angle $\theta = \pm 22^\circ$ where the corner and edge states have frequencies, 10.27 GHz and 10.18 GHz, respectively. The coupling between the edge and corner states is revealed using the pump-probe measurement schematically illustrated in the inset of Fig. 5g. The source is placed on the edge at the left side of the corner, while the detector is placed near the corner. The pump-probe spectroscopy in Fig. 5g shows that there are two corner modes within the bulk band gap (indicated by the two red arrows): one at 10.27 GHz, the other at 12.26 GHz. The corner mode at 10.27 GHz is very close to the edge band (indicated by the blue arrow). The hybridization between the edge and corner modes is manifested directly in the measured electric field profiles in Fig. 5h which are obtained by scanning the electric field at the two frequencies, 10.27 GHz and 12.26 GHz. The electric field profile measured at 12.26 GHz indicates a clear feature of evanescent wave excitation of a spectrally-isolated, strongly-localized corner mode. In contrast, the electric field profile measured at 10.27 GHz indicates visible

hybridization and coupling between the corner mode and the edge modes. Such coupled edge-corner system may serve as coupled waveguide-cavity systems in photonic chips.

Conclusion and outlook

In this work, we unveil twisting as a new degree-of-freedom toward higher-order topology in 2D dielectric, subwavelength PhCs. Here, the nonsymmorphic symmetry induced by twisting leads to anomalous quadrupole topology for photons. The intriguing properties of the photonic anomalous quadrupole topological insulators are revealed using a box-like structure comprised of two PhCs with opposite twisting angles. The photonic wavefunctions of the edge and corner states are directly visualized using the near-field scanning methods. Consistent theory and experiments show that the photonic and Wannier band gaps of the PhCs can be controlled effectively by the twisting degree-of-freedom. Consequently, rich edge and corner phenomena are observed when the twisting angle is tuned, demonstrating efficient photonic states transfer among 0D corner states, 1D edge states and 2D bulk states via twisting. Our study opens a new pathway toward twisting-photonics with higher-order topology and reconfigurable quadrupole topological photonic chips for future topological photonics.

Materials and Methods

Sample fabrication

In this work, all the samples were constructed by carefully pasting dielectric cylinders into a pre-printed drawing on which the location of each cylinder is marked. As the element of the sample, the dielectric cylinder is made of Al_2O_3 with permittivity 9.8 and has the height of 8.0 mm and the radius of 2.5 mm, all of which were fabricated by Smile Precision Ceramics Co. Ltd. (Shanghai).

Experimental setup

Two parallel metal plates cladding the sample constitute a quasi-2D space, with a 1.5mm air gap between the upper metal plate and the sample, for the convenience of shifting the sample and scanning fields. In addition, the absorbing sponges surround the sample in order to simulate the

open boundary condition. A monopole antenna, about 7 mm in height, is inserted through the lower plate as an excitation source. Another antenna as a detecting probe consisting of a coaxial cable with the exterior metal layer stripped away, is inserted through the upper plate, to measure the surface field of samples. We use a microwave vector network analyzer (PNA-N5203C) to record the magnitude and phase of the electromagnetic signal. In the scanning measurement, the lower plate is mounted on a translational stage with the scan step being 2.5mm. More details are provided in Supplementary Note 11.

Simulation

Numerical simulations are performed using a commercial finite-element simulation software (COMSOL MULTIPHYSICS) via the rf module. Most simulations are done for 2D transverse magnetic harmonic modes, while some simulations (in the Supplementary Note 2) is performed for the genuine 3D set-up.

Acknowledgements

Z.K.L and J.H.J are supported by the Jiangsu Province Specially-Appointed Professor Funding and the National Natural Science Foundation of China (Grant No. 11675116). Y.L is supported by National Natural Science Foundation of China (Nos. 11574226, 11704271, and 11874274). X.Z, W.L and B.H are supported by the National Natural Science Foundation of China (Grant No. 11474212).

Author contributions

J.H.J conceived the idea and initiated the project. J.H.J and B.H guided the research. J.H.J and Z.K.L established the theory. Z.K.L and X.Z performed the numerical calculations and simulations. X.Z, W.L and B.H achieved the experimental set-up and measurements. All the authors contributed to the discussions of the results and the manuscript preparation. J.H.J, X.Z, Z.K.L and B.H wrote the manuscript and the Supplementary Information.

Competing Interests

The authors declare that they have no competing financial interests.

Data availability

All data are available in the manuscript and the Supplementary Information. Additional information is available from the corresponding authors through proper request.

Code availability

We use the commercial software COMSOL MULTIPHYSICS to perform the simulation and calculations. Request to the details can be addressed to the corresponding authors.

References

- [1] Benalcazar, W. A., Bernevig, B. A. & Hughes, T. L. Quantized electric multipole insulators. *Science* **357**, 61-66 (2017).
- [2] Langbehn, J., Peng, Y., Trifunovic, L., von Oppen, F. & Brouwer, P. W. Reflection-symmetric second-order topological insulators and superconductors. *Phys. Rev. Lett.* **119**, 246401 (2017).
- [3] Song, Z. D., Fang, Z. & Fang, C. (d-2)-dimensional edge states of rotation symmetry protected topological states. *Phys. Rev. Lett.* **119**, 246402 (2017).
- [4] Benalcazar, W. A., Bernevig, B. A. & Hughes, T. L. Electric multipole moments, topological multipole moment pumping, and chiral hinge states in crystalline insulators. *Phys. Rev. B* **96**, 245115 (2017).
- [5] Schindler, F. *et al.* Higher-order topological insulators. *Sci. Adv.* **4**, eaat0346 (2018).
- [6] Ezawa, M. Higher-order topological insulators and semimetals on the breathing Kagome and pyrochlore lattices. *Phys. Rev. Lett.* **120**, 026801 (2018).

[7] Kunst, F. K., van Miert, G. & Bergholtz, E. J. Lattice models with exactly solvable topological hinge and corner states. *Phys. Rev. B* **97**, 241405(R) (2018).

[8] Franca, S., van den Brink, J. & Fulga, I. C. An anomalous higher-order topological insulator. *Phys. Rev. B* **98**, 201114 (2018).

[9] Xie, B. Y. *et al.* Second-order photonic topological insulator with corner states. *Phys. Rev. B* **98**, 205147 (2018).

[10] Serra-Garcia, M. *et al.* Observation of a phononic quadrupole topological insulator. *Nature* **555**, 342-345 (2018).

[11] Peterson, C. W., Benalcazar, W. A., Hughes, T. L. & Bahl, G. A quantized microwave quadrupole insulator with topological protected corner states. *Nature* **555**, 346-350 (2018).

[12] Imhof, S. *et al.* Topoelectrical circuit realization of topological corner modes. *Nat. Phys.* **14**, 925-929 (2018).

[13] Noh, J. *et al.* Topological protection of photonic mid-gap defect modes. *Nat. Photon.* **12**, 408-415 (2018).

[14] Schindler, F. *et al.* Higher-order topology in bismuth. *Nat. Phys.* **14**, 918-924 (2018).

[15] Xue, H., Yang, Y., Gao, F., Chong, Y. & Zhang, B. Acoustic higher-order topological insulator on a kagome lattice. *Nat. Mater.* **18**, 108-112 (2019).

[16] Ni, X., Weiner, M., Alù, A. & Khanikaev, A. B. Observation of higher-order topological acoustic states protected by generalized chiral symmetry. *Nat. Mater.* **18**, 113-120 (2019).

[17] Zhang, X. *et al.* Second-order topology and multi-dimensional topological transitions in sonic crystals. *Nat. Phys.* **15**, 582-588 (2019).

[18] Zhang, X. *et al.* Symmetry-protected hierarchy of anomalous topological multipoles in nonsymmorphic metacrystals. Preprint at <https://www.arXiv.org/abs/1811.05514>.

[19] Mittal, S., Orre, V. V., Zhu, G., Gorlach, M. A., Poddubny, A. & Hafezi, M. Photonic quadrupole topological phases. *Nat. Photon.* **13**, 692-696 (2019).

[20] Hassan, A. E., Kunst, F. K., Moritz, A., Andler, G., Bergholtz, E. J. & Bourennane, M. Corner states of light in photonic waveguides. *Nat. Photon.* **13**, 697-700 (2019).

[21] Chen, X.-D. *et al.* Direct observation of corner states in second-order topological photonic crystal slabs. *Phys. Rev. Lett.* **122**, 233902 (2019).

[22] Xie, B.-Y. *et al.* Visualization of higher-order topological insulating phases in two-dimensional dielectric photonic crystals. *Phys. Rev. Lett.* **122**, 233903 (2019).

[23] Ota, Y. *et al.* Photonic crystal nanocavity based on a topological corner state. *Optica* **6**, 786-789 (2019).

[24] Liu, Y. *et al.* Topological corner modes in a brick lattice with nonsymmorphic symmetry. Preprint at <https://www.arXiv.org/abs/1812.11846>.

[25] Zhang, L. *et al.* Higher-order photonic topological states in surface-wave photonic crystals. Preprint at <https://www.arXiv.org/abs/1901.07154>

[26] Lin, M. and Hughes, T. L. Topological quadrupolar semimetals. *Phys. Rev. B* **98**, 241103 (2018).

[27] Hasan, M. Z. & Kane, C. L. Colloquium: topological insulators. *Rev. Mod. Phys.* **82**, 3045-3067 (2010).

[28] Qi, X.-L. & Zhang, S.-C. Topological insulators and superconductors. *Rev. Mod. Phys.* **83**, 1057-1110 (2011).

[29] Li, G. *et al.* Observation of van Hove singularities in twisted graphene layers. *Nat. Phys.* **6**, 109-113 (2010).

[30] Y. Cao *et al.* Correlated insulator behaviour at half-filling in magic-angle graphene superlattices. *Nature* **556**, 80-84 (2018).

[31] Y. Cao *et al.* Unconventional superconductivity in magic-angle graphene superlattices. *Nature* **556**, 43-50 (2018).

[32] Wang, Z., Chong, Y., Joannopoulos, J. D. & Soljacic, M. Observation of unidirectional backscattering immune topological electromagnetic states. *Nature* **461**, 772-775 (2009).

[33] Hafezi, M., Demler, E. A., Lukin, M. D. & Taylor, J. M. Robust optical delay lines with topological protection. *Nat. Phys.* **7**, 907-912 (2011).

[34] Poo, Y., Wu, R., Lin, Z., Yang, Y. & Chan, C. T. Experimental realization of self-guiding unidirectional electromagnetic edge states. *Phys. Rev. Lett.* **106**, 093903 (2011).

[35] Kraus, Y. E., Lahini, Y., Ringel, Z., Verbin, M. & Zilberberg, O. Topological states and adiabatic pumping in quasicrystals. *Phys. Rev. Lett.* **109**, 106402 (2012).

[36] Hafezi, M., Mittal, S., Fan, J., Migdall, A. & Taylor, J. M. Imaging topological edge states in silicon photonics. *Nat. Photon.* **7**, 1001-1005 (2013).

[37] Khanikaev, A. B. *et al.* Photonic topological insulators. *Nat. Mater.* **12**, 233–239 (2013).

[38] Rechtsman, M. C. *et al.* Photonic Floquet topological insulators. *Nature* **496**, 196-200 (2013).

[39] Chen, W.-J. *et al.* Experimental realization of photonic topological insulator in a uniaxial metacrystal waveguide. *Nat. Commun.* **5**, 6782 (2014).

[40] Lu, L., Joannopoulos, J. D. & Soljacic, M. Topological photonics. *Nat. Photon.* **8**, 821-829 (2014).

[41] Cheng, X. *et al.* Robust reconfigurable electromagnetic pathways within a photonic topological insulator. *Nat. Mater.* **15**, 542-548 (2016).

[42] Gao, F. *et al.* Probing topological protection using a designer surface plasmon structure. *Nat. Commun.* **7**, 11619 (2016).

[43] Maczewsky, L. J., Zeuner, J. M., Nolte, S. & Szameit, A. Observation of photonic anomalous Floquet topological insulators. *Nat. Commun.* **8**, 13756 (2017).

[44] Barik, S. *et al.* A topological quantum optics interface. *Science* **359**, 666-668 (2018).

[45] Yang, Y. *et al.* Visualization of a unidirectional electromagnetic waveguide using topological photonic crystals made of dielectric materials. *Phys. Rev. Lett.* **120**, 217401 (2018).

[46] Li, F.-F. *et al.* Topological light-trapping on a dislocation. *Nat. Commun.* **9**, 2462 (2018).

[47] Yang, Y. *et al.* Realization of a three-dimensional photonic topological insulator. *Nature* **565**, 622-626 (2019).

[48] Ozawa, T. *et al.* Topological photonics. *Rev. Mod. Phys.* **91**, 015006 (2019).

[49] Wang, H.-X., Guo, G.-Y. & Jiang, J.-H. Band topology in classical waves: Wilson-loop approach to topological numbers and fragile topology. *New J. Phys.* **21**, 093029 (2019).